

University of Groningen

## Energy- and charge-state-resolved spectrometry of tin laser-produced plasma using a retarding field energy analyzer

Poirier, L.; Lassise, A.; Mostafa, Y.; Behnke, L.; Braaksma, N.; Assink, L.; Hoekstra, R.; Versolato, O. O.

*Published in:*  
Applied Physics B: Lasers and Optics

*DOI:*  
[10.1007/s00340-022-07844-5](https://doi.org/10.1007/s00340-022-07844-5)

**IMPORTANT NOTE: You are advised to consult the publisher's version (publisher's PDF) if you wish to cite from it. Please check the document version below.**

*Document Version*  
Publisher's PDF, also known as Version of record

*Publication date:*  
2022

[Link to publication in University of Groningen/UMCG research database](#)

### *Citation for published version (APA):*

Poirier, L., Lassise, A., Mostafa, Y., Behnke, L., Braaksma, N., Assink, L., Hoekstra, R., & Versolato, O. O. (2022). Energy- and charge-state-resolved spectrometry of tin laser-produced plasma using a retarding field energy analyzer. *Applied Physics B: Lasers and Optics*, 128(7), [135]. <https://doi.org/10.1007/s00340-022-07844-5>

### **Copyright**

Other than for strictly personal use, it is not permitted to download or to forward/distribute the text or part of it without the consent of the author(s) and/or copyright holder(s), unless the work is under an open content license (like Creative Commons).

The publication may also be distributed here under the terms of Article 25fa of the Dutch Copyright Act, indicated by the "Taverne" license. More information can be found on the University of Groningen website: <https://www.rug.nl/library/open-access/self-archiving-pure/taverne-amendment>.

### **Take-down policy**

If you believe that this document breaches copyright please contact us providing details, and we will remove access to the work immediately and investigate your claim.

Downloaded from the University of Groningen/UMCG research database (Pure): <http://www.rug.nl/research/portal>. For technical reasons the number of authors shown on this cover page is limited to 10 maximum.



# Energy- and charge-state-resolved spectrometry of tin laser-produced plasma using a retarding field energy analyzer

L. Poirier<sup>1,2</sup> · A. Lassise<sup>1</sup> · Y. Mostafa<sup>1,2</sup> · L. Behnke<sup>1,2</sup> · N. Braaksma<sup>3</sup> · L. Assink<sup>1,4</sup> · R. Hoekstra<sup>1,4</sup> · O. O. Versolato<sup>1,2</sup>

Received: 6 February 2022 / Accepted: 14 May 2022 / Published online: 28 June 2022  
© The Author(s) 2022

## Abstract

We present a method to obtain the individual charge-state-dependent kinetic-energy distributions of tin ions emanating from a laser-produced plasma from their joint overlapping energy distributions measured by means of a retarding field energy analyzer (RFA). The method of extracting charge state specific parameters from the ion signals is described mathematically, and reinforced with experimental results. The absolute charge-state-resolved ion energy distributions is obtained from ns-pulse Nd:YAG-laser-produced microdroplet tin plasmas in a setting relevant for state-of-the-art extreme ultraviolet nanolithography.

## 1 Introduction

Laser-produced plasmas (LPP) are a topic of interest for their ability to efficiently produce extreme ultraviolet (EUV) and soft x-ray radiation. In state-of-the-art LPP nanolithography, the production of 13.5 nm EUV light is carried out by a high-repetition-rate tin plasma, driven by a  $\sim 10^{10}$  W/cm<sup>2</sup>, 50 kHz pulsed CO<sub>2</sub> laser. Multiply charged tin ions Sn<sup>8+</sup>–Sn<sup>14+</sup> are responsible for the EUV emission [1]: those ions display overlapping and narrow unresolved transition arrays (UTAs) around 13.5 nm in singly-, doubly- and triply-excited states [2]. Multilayer mirror optics (MLM) are used to collect and guide the EUV radiation emitted by the plasma. A MLM consisting of a series of alternating thin Mo and Si layers gives rise to a  $\sim 70\%$  reflection coefficient at 13.5 nm wavelength in a 2% reflection bandwidth [3, 4]. As the hot and dense LPP expands in the source chamber, the mirrors are subject to a gradual reduction of optical properties when

fast tin ions and neutral atoms collide with their surfaces. Various processes such as implantation, sputtering and coating are responsible for the degradation of the overall efficiency of the optics. The type of damage is contingent on the kinetic energy and charge of the ions [5].

For this purpose the ion emission characteristics need to be understood, in particular the charge state, the kinetic energy and angular distribution. The quantification of ion emission is key to establish the energy balance of the different channels through which the energy of the LPP is dissipated.

A wide variety of ion diagnostic tools has been used in the literature, e.g., electrostatic probes [6]; charge-integrated Faraday cups (FC) [7, 8]; charge-resolved retarding field analyzers (RFA) [9, 10]; electrostatic analyzers (ESA) [11–15]; and Thompson parabolas (TPS) [16]. Recently, the ARCNL ESA was cross-calibrated with a 4-grid FC, in an effort to produce high-accuracy charge-resolved ion spectra [11]. To study the angular dependence of the ion flow, such a spectrometer is not befitting given its dimensions, weight and particulars of its precise alignment to the plasma. This angular dependence can instead be more elegantly obtained using simple, robust and easy-to-align RFAs. Placing RFA detectors at various angles around the LPP allows for the simultaneous measurement of ion spectra, delivering valuable information on the angular dependence of the charge-energy spectra of the emitted ions. The prime shortcoming of the RFA type of detectors is their limited resolution when compared to the ESA. However, as we will show, the energy resolution obtained from commercially available RFAs (see

✉ O. O. Versolato  
o.versolato@arcnl.nl

<sup>1</sup> Advanced Research Center for Nanolithography (ARCNL), Science Park 106, 1098 XG Amsterdam, The Netherlands

<sup>2</sup> Department of Physics and Astronomy and LaserLab, Vrije Universiteit Amsterdam, De Boelelaan 1081, 1081 HV Amsterdam, The Netherlands

<sup>3</sup> ASML US LP, 17075 Thornmint Ct, San Diego, California 92127, USA

<sup>4</sup> Zernike Institute for Advanced Materials, University of Groningen, Nijenborgh 4, 9747 AG Groningen, The Netherlands

Appendix) is sufficient to discriminate all here relevant charge states.

The present survey aims to develop and demonstrate methods to obtain charge-energy resolved spectra from a 4-grid Kimball Physics FC-73 RFA used to diagnose our tin laser-produced plasma. In these plasmas, a plurality of charge states and kinetic energies are produced nearly instantaneously by the impact of the 10-ns-long pulses of a Nd:YAG laser onto a tin microdroplet. The experimental setup is first described. Next, the retarding field analysis approach is expounded and illustrated. Finally, a reconstructed charge-resolved RFA spectrum is presented.

## 2 Experimental setup

### 2.1 Laser-produced plasma (LPP)

Our LPP EUV source and auxiliary equipment has been described in detail before [17]. The components most relevant to this work are briefly recalled here, see also Fig. 1. A tin reservoir is mounted on top of a vacuum chamber (10<sup>-7</sup> mbar) and is kept at a constant temperature of 260 °C.

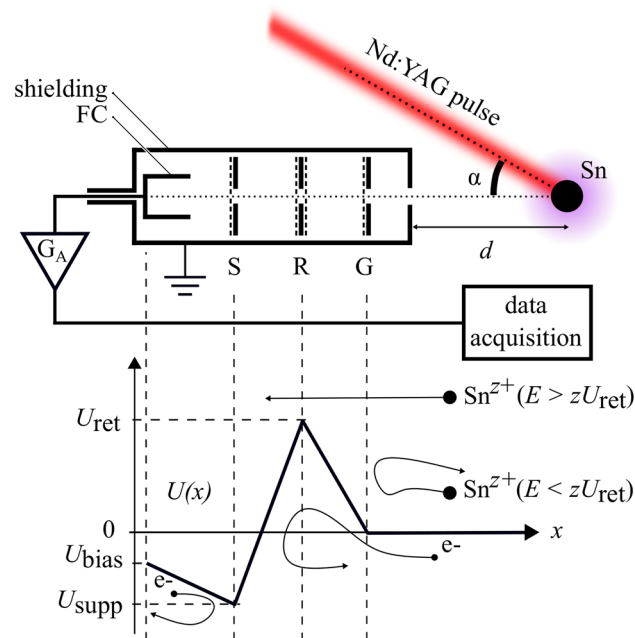


**Fig. 1** A tin droplet is converted to plasma using a 1064 nm, 10 ns-long Nd:YAG laser pulse. An RFA is placed at  $d = 445$  mm from the plasma, at an angle  $\alpha = 41.4^\circ$  with respect to the laser direction. Inside the RFA, the plasma ions traverse four grids: one grounding grid (G), two retarding grids (R) and a suppressor grid (S). The ion current on the FC is amplified by a fast trans-impedance amplifier ( $G_A$ ). In the bottom panel the corresponding electrostatic potentials are schematically shown (black line). The behaviour of plasma ions, plasma electrons, and secondary electrons is also sketched

From the reservoir, a nozzle produces a 22 kHz droplet train of pure, molten tin droplets traveling along the vertical axis of the vacuum chamber. The microdroplets, which have a diameter of 38  $\mu\text{m}$ , first traverse a horizontal light sheet produced from a helium-neon laser. The light scattered off of the Sn droplets is detected by a photo-multiplier tube. The detected signal is frequency down-converted to 10 Hz to enable triggering of the laser system that creates the plasma. This Nd:YAG laser system produces pulses at a wavelength of 1064 nm and a time duration at full-width at half-maximum (FWHM) of approximately 10 ns. The beam is focused to a Gaussian spot (100  $\mu\text{m}$  FWHM) onto the droplets in the center of the chamber. By using a half-wave plate and a thin-film polarizer, the laser pulse energy can be adjusted without affecting the spatial beam profile. In the following, the laser pulse energy was set to 90 mJ.

### 2.2 The retarding field energy analyzer (RFA)

The RFA is placed at a distance  $d = 445$  mm from the LPP, at an angle  $\alpha = 41.4^\circ$  with respect to the direction of the incoming laser light, as depicted schematically in Fig. 1. The entrance aperture of the RFA has a 5.0 mm diameter leading to a solid angle of  $\Delta\Omega = 99 \mu\text{sr}$ . The FC in which the ion current is collected, is biased to  $U_{\text{bias}} = -30$  V while the suppression grid is held at  $U_{\text{supp}} = -100$  V.

The retarding grid bias  $U_{\text{ret}}$  is varied in steps of 20 V between (set) voltages of 10 and 500 V with actual read voltages used in the analysis (and shown in selected traces in Fig. 2) to create a potential barrier to reject ions with an energy  $E < zeU_{\text{ret}}$ , with  $z$  the charge state of the incoming  $\text{Sn}^{z+}$  ion. At the maximum voltage the ion current signal in the FC was found to be fully suppressed. In the time traces of

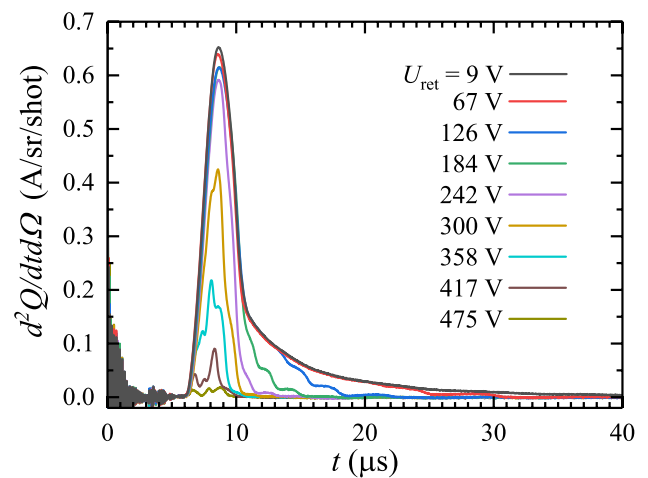


**Fig. 2** Typical ion current traces as recorded by the RFA for different values of retarding voltage. Smooth steps appear in the time-of-flight traces as the retarding voltage is increased

the ion current, the ringing at  $t = 0$  s in Fig. 2 is due to pick-up of the main laser's Q-switch and due to signal accredited to energetic photoelectrons emitted from the Faraday cup. The small noisy feature around  $4 \mu\text{s}$  is due to pick-up from the shadowgraphy laser system (see Sect. 3) and will lead to tiny high-energy ( $\sim 5 - 8$  keV) features in the later spectra.

Each of the four grids has a geometrical transmission of 83%, as calculated from the pitch and the wire diameter. Assuming an alignment of the grids where the grids are spaced such that they have minimal geometric overlap but the same orientation, the total transmission may be estimated to be 41%. This figure was previously found to be consistent with an ion current comparison between the RFA and a grid-less Faraday cup [11].

We convert the RFA time-of-flight (ToF) current traces to a voltage using a trans-impedance amplifier with a gain of 25 kV/A and a bandwidth of 25 MHz. The amplifier consists of two stages. The first, a trans-impedance stage with 5 kV/A gain, is based on a high speed operational amplifier (Texas Instruments OPA847) with a low input current noise of  $2.5 \text{ pA}/\sqrt{\text{Hz}}$  and a gain bandwidth product of 3 GHz. This stage is followed by a non-inverting output stage (Texas Instruments OPA691) with tenfold amplification. The output impedance of the amplifier is  $50 \Omega$ , matched to the load of the amplifier, giving rise to the 25 kV/A gain. Due to the fast response of the amplifier, deconvolution of the measured signal from the measurement electronics is not necessary to accurately reflect the ion current impinging upon the collector.

In a previous experiment [11], we confirmed the gain of the trans-impedance amplifier to be equal to its expected value of 25 kV/A. Measured ion transients have a typical duration on the order of several  $10 \mu\text{s}$ . Our amplifier, providing an amplified capacitive readout of the RFA, was designed accordingly to have a fast current ramp-up ( $\sim \text{ns}$ ) and a particularly slow (negative) charge re-flow ( $\sim \text{ms}$ ).

### 3 Method of data processing

The post-processing of RFA data aims at constructing the charge-resolved ion energy distributions from the ToF current measurements taken at various retarding voltages. First, average ion currents are calculated for each retarding voltage setting. In the experiments presented here, 200 shots are recorded for each retarding voltage value. Outliers, attributable to limited laser-to-droplet alignment accuracy, are removed before averaging. For this purpose, concurrently recorded shadowgraphic images of the tin target are used. The shadowgraphy imaging setup is described in earlier studies (see, e.g. [17, 18]) and enables obtaining the velocity of the plasma-propelled liquid

mass. This propulsion velocity is a convenient metric for laser-to-droplet alignment [19]. For each shot, we extract the propulsion speed; in the rest of the analysis we only consider the shots where the propulsion speed is comprised within  $\pm 5\%$  of the most likely propulsion speed. For the presented data, about 75% of the shots are sufficiently well aligned.

The baseline of the signal is evaluated at late times ( $> 100 \mu\text{s}$ ), and is subtracted from each of the average current transient to correct for any potential drift in the baseline. This baseline subtraction also provides a first-order correction for re-flow current due to the capacitive readout (with the re-flow occurring at  $\sim \text{ms}$  time scale). The ion current is averaged over the small solid angle defined by the FC aperture and its distance to the plasma.

$$\frac{d^2 Q(t)}{dt d\Omega} \approx \frac{dQ(t)}{dt} \frac{1}{\Delta\Omega}. \quad (1)$$

We omit the solid angle double differential notation for clarity in the following.

The time domain ion current  $\frac{dQ(t)}{dt}$  is next expressed as energy domain current  $\frac{dQ(E)}{dE}$ , given that the RFA selectively transmits ions based on their charge state and energy  $E$ , through

$$\frac{dQ(E)}{dE} = \frac{dQ(t)}{dt} \frac{dt}{dE}. \quad (2)$$

For each retardation voltage  $U_{\text{ret}}$  applied, we split the ion current traces in the energy domain into energy bins of width  $eU_{\text{ret}}$ . We assign the index  $n$  to the energy bin spanning  $neU_{\text{ret}}$  to  $(n+1)eU_{\text{ret}}$ , centered at  $E_n = \left(n + \frac{1}{2}\right)eU_{\text{ret}}$ , containing a charge  $Q_n$

$$Q_n(E_n) = \int_{neU_{\text{ret}}}^{(n+1)eU_{\text{ret}}} \frac{dQ(E)}{dE} dE. \quad (3)$$

The charge contribution to the discretized ion energy distribution  $dQ_n(E)/dE$  from the  $n$ -th bin is given by

$$\frac{dQ_n(E_n)}{dE} \approx \frac{Q_n(E_n)}{\Delta E} = \frac{Q_n(E_n)}{eU_{\text{ret}}}, \quad (4)$$

with the integration region  $\Delta E = (n+1)eU_{\text{ret}} - neU_{\text{ret}} = eU_{\text{ret}}$ . The discretized ion energy distribution is constructed considering data from all scanned  $U_{\text{ret}}$  values and is transformed into a continuous function by linear interpolation.

Each bin  $n$  contains contributions from charge states  $z = 1$  through  $z = n$ . Ions in charge state  $z = n+1$  that pass the retardation grid with its voltage  $U_{\text{ret}}$  will end up in bin  $n+1$  (see Fig. 3). Thus,

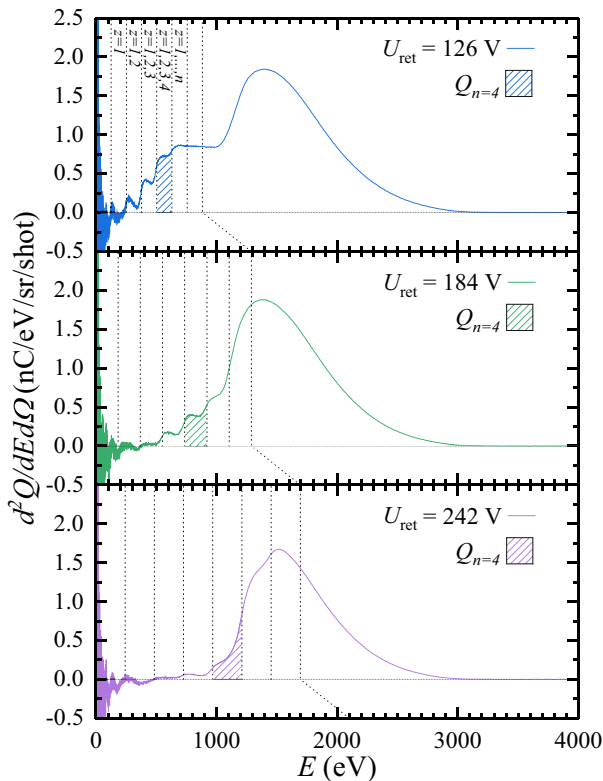


**Fig. 3** Three sample ion current transients for non-consecutive  $U_{\text{ret}}$  values are presented in the energy-domain. The charge  $Q_n$  collected in the  $n$ -th energy bin of  $d^2Q(E)/dEd\Omega$ , spanning the range from  $E = neU_{\text{ret}}$  to  $E = (n + 1)eU_{\text{ret}}$  (dotted vertical lines), is pictured by the hatched area. It contains ions with charge state  $z \leq n$

$$Q_n = \sum_{z \leq n} Q_n^z. \tag{5}$$

(We note that the individual ion charge  $Q_n^z$ , with superscript  $z$  denoting the charge state, is related to ion number  $N_n^z$  through  $Q_n^z = zeN_n^z$ .) The identity Eq. (5) enables to iteratively obtain charge-state-resolved energy distributions  $dQ^z(E)/dE$ . Starting with  $z = 1$ , we can take directly  $dQ^{z=1}/dE = dQ_{n=1}(E)/dE$  as it is the only ion charge contributing to bin  $n = 1$ . The energy spectrum of the next charge state  $z = 2$  is obtained subtracting the now known spectrum of the  $z = 1$  charge from the  $n = 2$  bin, *et cetera*:

$$\frac{dQ^z(E)}{dE} = \frac{dQ_{n=z}(E)}{dE} - \frac{dQ_{n=z-1}(E)}{dE}. \tag{6}$$

The energy spectrum of any ion charge state can thus be obtained from this bottom-up procedure.

Once all of the  $dQ^z(E)/dE$  terms are calculated, the charge-integrated spectrum  $dQ(E)/dE$  is assembled:

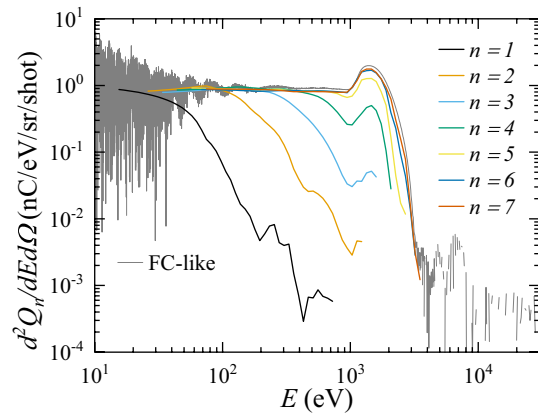


**Fig. 4** Cumulative energy distributions; the  $n$ -wise spectra ( $n = 1 - 7$ ) are shown in different colors. The highest-index cumulative distribution  $dQ_{n=7}/dE$  overlaps with the charge-integrated FC-like spectrum (gray line)

$$\frac{dQ(E)}{dE} = \sum_{z \leq z_{\text{max}}} \frac{dQ^z(E)}{dE} = \frac{dQ_{n=z_{\text{max}}}(E)}{dE}. \tag{7}$$

Here the maximum ion charge  $z_{\text{max}}$  (and with it, the maximum bin number  $n_{\text{max}}$ ) is introduced to truncate the iterative procedure. Its value should be set to be no larger than the maximum charge state expected to be emitted from the plasma in significant numbers. Setting  $z_{\text{max}}$  to a larger value will lead to increased post-processing computational time and the energy distributions of the highest charge-states will in any case be dominated by noise. If the maximum charge state  $z_{\text{max}}$  is set right, the charge-integrated spectrum  $dQ/dE$  determined through Eq. (7) will overlap closely with the corresponding charge-energy spectrum measured without any retarding potential applied (or, equivalently, for the lowest value of  $U_{\text{ret}}$  applied), transforming the full current via Eq. (2).

### 4 RFA spectrum

Next we apply the method to the case at hand. A maximum charge state of  $z = 7$  was determined to describe sufficiently well the ion currents for the experiment presented here. Higher charge states are also present in the hot and dense phase of the plasma, as is known from spectroscopy in the extreme ultraviolet range (see e.g. Refs. [2, 20, 21]), where spectroscopic features are assigned to  $\text{Sn}^{z+}$  ions in higher charge states up to  $z = 14$ . However such higher charge states recombine with plasma electrons close to the laser-matter interaction zone, shifting the charge state distribution

down to produce the  $\text{Sn}^{z+}$  ions in lower charge states as observed here.

Figures 4 and 5 show the cumulative [Eq. (4)] and charge-state-resolved energy distributions [Eq. (6)] of  $\text{Sn}^{z+}$  ions of the current experiment, respectively. In both figures, the gray line corresponds to a charge-integrated, Faraday cup type (FC-like) spectrum calculated from the corresponding time-of-flight trace via Eq. (7). Specifically, the FC-like spectrum is derived from the RFA current measured for the lowest retardation grid voltage of  $U_{\text{ret}} = 9$  V. Note that the RFA and FC-like data were thus taken with the same device. As there is no significant contribution to the current trace of energies below  $eU_{\text{ret}} = 9$  eV, the FC-like signal closely resembles the total current that would be measured from a regular Faraday cup without any retardation voltage.

In Fig. 5, the dashed gray line indicates the noise level of the FC-like spectrum, evaluated using the standard deviation of the ion current at late times (typically between 100–200  $\mu\text{s}$  where there are no discernible features in the ToF signal). It can be shown analytically that the noise level scales with  $E^{-3/2}$  considering the  $dt/dE$  term in Eq. (2) ( $dE/dt \sim d(1/t^2)/dt \sim 1/t^3 \sim E^{3/2}$ ) and assuming white noise in the time-of-flight traces with a time-independent noise amplitude.

The FC-like spectrum exhibits a high-energy peak between 1 and 2 keV. This high-energy peak has recently been attributed to a quasi-spherical expanding shell formed at early times in the plasma expansion into which subsequent hotter plasma is bunched—an effect that is characteristic to temporally Gaussian-shaped laser pulses [22].

In Fig. 5 the charge-integrated spectrum  $dQ/dE$  determined through Eq. (7) is found to closely match with the corresponding charge-energy spectrum measured without

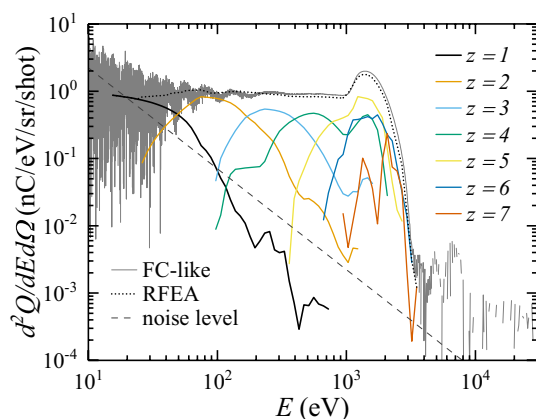


**Fig. 5** Charge-resolved energy distributions; the  $z$ -wise spectra ( $z = 1 - 7$ ) are shown in different colors. The sum of the charge-resolved spectra  $dQ/dE$  overlaps with the charge-integrated FC-like spectrum (gray line). The estimated noise level of the FC-like current trace is pictured by the transversal gray dashed line ( $\propto E^{-3/2}$ )

any retarding potential applied (FC-like), supporting the robustness of the method as well as the choice of the largest considered charge state  $z_{\text{max}} = 7$ . Ions with higher charge may still be present but at negligible quantities. The individual charge-energy spectra follow trends similar to those seen previously using an electrostatic time-of-flight analyzer [11, 22], with in particular the higher charge states bunching up to form the aforementioned high-energy peak.

## 5 Conclusion

A method is presented to interpret data obtained from a retarding field analyzer (RFA). The process enables one to obtain the individual charge-state dependent kinetic-energy distributions of tin ions emanating from a laser-produced plasma from their overlapping energy distributions. Our method uses the fact that ions with the same energy but different charge state are selectively filtered out in the time-of-flight current signal by the applied retarding potential, which is scanned to obtain complete energy distributions. The selective filtering enables obtaining the individual charge state energy spectra in an iterative manner. This so-called “bottom-up” approach starts out from identifying the energy intervals where only a single—the lowest—charge state  $z = 1$  contributes. Subsequently, the higher charge states ( $z = 2, 3, et\ cetera$ ) are step-wise identified.

Applying our method to the obtained data from ns-laser-pulse impact on a tin microdroplet, we find that the individual charge-energy spectra follow trends similar to those seen previously using an electrostatic time-of-flight analyzer, with a characteristic high-energy peak comprising bunched charge states.

The understanding of complete spatial ion emission characteristics is crucial for establishing the momentum and energy balance of the LPP, as well as for designing ion “debris” mitigation schemes in future sources of EUV light for nanolithography. Our bottom-up method will facilitate obtaining angularly resolved charge-energy distributions from RFA measurements, as the robust and compact RFAs can conveniently be arranged around an LPP vacuum vessel.

## Appendix : Energy resolution

To assess the energy resolution of an RFA we next analyze the energy-derivative of the  $dQ/dE$  traces as obtained from the oscilloscope using Eq. (2). This derivative  $d^2Q/dE^2$  exhibits Gaussian peaks originating from the smooth, step wise increment of contributing charge states to the next bin (cf. Fig. 3) as is clear from Fig. 6.a, where  $d^2Q(E)/dE^2$  is shown for a retarding voltage of 106 V. The widths of these Gaussian peaks give access to the experimental resolution of

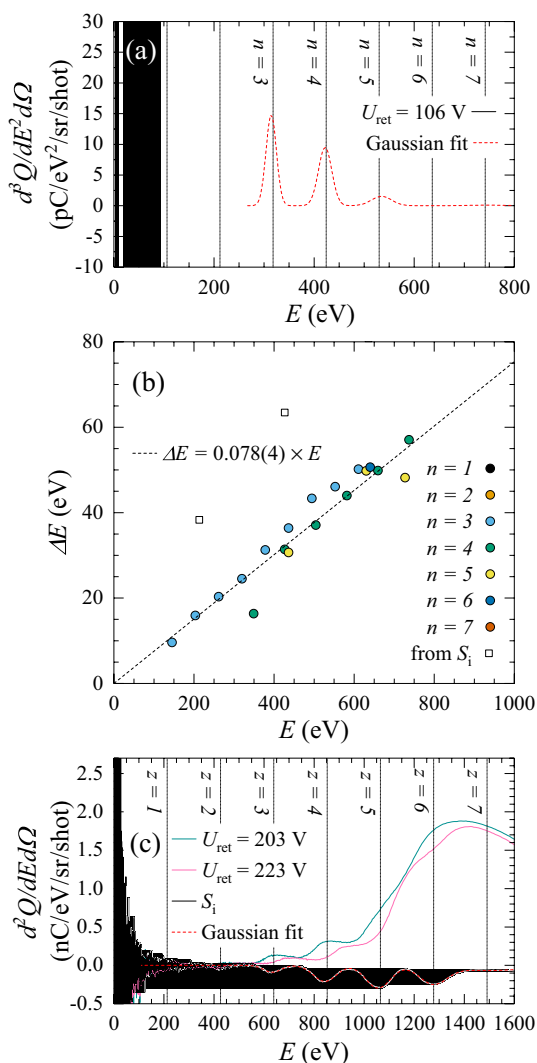


**Fig. 6** In panel (a) the derivative of the energy-domain ion energy distribution (black line) is fitted with Gaussian peaks (red dashed line) centered around energies equal to multiples of the retarding voltage  $eU_{\text{ret}}$ . The data below 250 eV was not included in the fitting range because of the low signal-to-noise level. The fitted widths of all valid peaks are reported in panel (b) (colored circles), where a linear trend is observed and fitted (dashed black line); the relative energy resolution  $\Delta E(E)/E$  is found to be 0.078(4). In panel (c), the differential signal  $S_i$  (black line) and its parent ion distributions (teal and pink lines) are represented.  $S_i$  shows peaks around multiples of the average retarding voltage  $E_i$ . Each differential peak corresponds to a specific charge state  $z$ ;  $S_i$  is also fitted with a 7-Gaussian array (red dashed line). Accurately fitted widths are also reported in panel (b) (black squares)

the RFA under actual operating conditions. Peaks from  $n = 3$  to  $n = z_{\text{max}} = 7$  can reliably be fitted with Gaussian functions. The widths are retrieved from the fits, while obvious outliers are removed. Figure 6.b presents the thus obtained

widths  $\Delta E$ , defined as the FWHM of the Gaussian peaks. As predicted by Sakai *et al.* [23], we find a constant ratio  $\Delta E/E$  here with a value of approximately 8%. Given the design of the aperture and grids of our RFA, Sakai *et al.* predict a smaller resolution of 2% for an idealized 2-grid RFA impinged on by a single-isotope, single-charge state, mono-energetic beam. We attribute the difference between the predicted and experimentally obtained resolution mainly to the presence of a wide range of tin isotopes and charge states, and to effects from the additional grids and their relative alignment.

The energy resolution can also be derived through a separate method which yields a consistent resolution of  $\Delta E/E \approx 9\%$ . This method is based on taking the difference between traces obtained from consecutive values of the retarding field  $U_{\text{ret}}^{i+1}$  and  $U_{\text{ret}}^i$ :  $S_i(E) = dQ_{i+1}(E)/dE - dQ_i(E)/dE$ , where  $i$  stands for the index of the  $U_{\text{ret}}$  increments.  $S_i$  also presents peaks centered at energies that are multiple of  $E_i = \frac{1}{2}e(U_{\text{ret}}^{i+1} + U_{\text{ret}}^i)$ . In Fig. 6c, vertical lines depict multiples of  $E_i$  on the energy axis, where contributions from the individual charge states manifest. If the retarding voltage increment  $U_{\text{ret}}^{i+1} - U_{\text{ret}}^i$  is small with respect to the local value of the resolution  $\Delta E$ , the convolution of the step size with the energy resolution provides Gaussian peaks. Fitting those peaks enables recovering energy resolution  $\Delta E(E)$ . In Fig. 6b, the widths of the  $S_i$  peaks corresponding to  $z = 2$  and 3 are shown to be slightly offset (at  $\sim 20$  eV) from the results from the more detailed first method, as was expected given that  $U_{\text{ret}}^{i+1} - U_{\text{ret}}^i = 20$  V in our scans, and to follow a similar slope  $\Delta E/E$  yielding the instrument resolution.

**Acknowledgements** The authors thank Duncan Verheijde for his support in understanding and improving the ESA-ToF electronics and analysis systematics. They also thank Jorijn Kuster for designing efficient and user-friendly software interfaces for our experimental setups. This work has been carried out at the Advanced Research Center for Nanolithography (ARCNL), a public-private partnership of the University of Amsterdam (UvA), the Vrije Universiteit Amsterdam, the Dutch Research Council (NWO) and the semiconductor equipment manufacturer ASML. This project has received funding from European Research Council (ERC) Starting Grant number 802648. This publication is part of the project New Light for Nanolithography (with project number 15697) of the research programme VIDI which is (partly) financed by the Dutch Research Council.

**Open Access** This article is licensed under a Creative Commons Attribution 4.0 International License, which permits use, sharing, adaptation, distribution and reproduction in any medium or format, as long as you give appropriate credit to the original author(s) and the source, provide a link to the Creative Commons licence, and indicate if changes were made. The images or other third party material in this article are included in the article's Creative Commons licence, unless indicated otherwise in a credit line to the material. If material is not included in the article's Creative Commons licence and your intended use is not permitted by statutory regulation or exceeds the permitted use, you will need to obtain permission directly from the copyright holder. To view a copy of this licence, visit <http://creativecommons.org/licenses/by/4.0/>.

## References

- G. O'Sullivan, B. Li, R. D'Arcy, P. Dunne, P. Hayden, D. Kilbane, T. McCormack, H. Ohashi, F. O'Reilly, P. Sheridan, E. Sokell, C. Suzuki, T. Higashiguchi, Spectroscopy of highly charged ions and its relevance to EUV and soft x-ray source development. *J. Phys. B* **48**(14), 144025 (2015)
- F. Torretti, J. Sheil, R. Schupp, M. Basko, M. Bayraktar, R. Meijer, S. Witte, W. Ubachs, R. Hoekstra, O.O. Versolato, A. Neukirch, J. Colgan, Prominent radiative contributions from multiply-excited states in laser-produced tin plasma for nanolithography. *Nat. Commun.* **11**(1), 1 (2020)
- S. Bajt, J.B. Alameda, T.W. Barbee Jr., W.M. Clift, J.A. Folta, B. Kaufmann, E.A. Spiller, Improved reflectance and stability of Mo-Si multilayers. *Opt. Eng.* **41**(8), 1797 (2002)
- Q. Huang, V. Medvedev, R. van de Kruijs, A. Yakshin, E. Louis, F. Bijkerk, Spectral tailoring of nanoscale EUV and soft x-ray multilayer optics. *Appl. Phys. Rev.* **4**(1), 011104 (2017)
- V. Bakshi (ed.), *EUV Lithography*, 2nd edn. (SPIE Press, 2018)
- M. Brandstätter, M. Weber, R. Abhari, Non-axisymmetric droplet irradiation effects on ion and extreme ultraviolet light emission of laser-produced plasma light sources. *J. Appl. Phys.* **129**(23), 233306 (2021)
- M.J. Deuzeman, A.S. Stodolna, E.E.B. Leerssen, A. Antoncicchi, N. Spook, T. Kleijntjens, J. Versluis, S. Witte, K.S.E. Eikema, W. Ubachs, R. Hoekstra, O.O. Versolato, Ion distribution and ablation depth measurements of a fs-ps laser-irradiated solid tin target. *J. Appl. Phys.* **121**(10), 103301 (2017)
- A. Bayerle, M. J. Deuzeman, S. van der Heijden, D. Kurilovich, T. de Faria Pinto, A. Stodolna, S. Witte, K. S. E. Eikema, W. Ubachs, R. Hoekstra, O. O. Versolato, Sn ion energy distributions of ns- and ps-laser produced plasmas. *Plasma Sources Sci. Technol.* **27**(4), 045001 (2018)
- I.V. Fomenkov, D.C. Brandt, A.N. Bykanov, A.I. Ershov, W.N. Partlo, D.W. Myers, N.R. Böwering, N.R. Farrar, G.O. Vaschenko, O.V. Khodykin, J.R. Hoffman, C.P. Chrobak, S.N. Srivastava, D.J. Golich, D.A. Vidusek, S.D. Dea, R.R. Hou, in *Alternative Lithographic Technologies*, vol. 7271 (International Society for Optics and Photonics, 2009), vol. 7271, pp. 852 – 863
- P. Yeates, C. Fallon, E.T. Kennedy, J.T. Costello, Charge resolved electrostatic diagnostic of colliding copper laser plasma plumes. *Phys. Plasmas* **18**(10), 103104 (2011)
- L. Poirier, A. Bayerle, A. Lassise, F. Torretti, R. Schupp, L. Benhke, Y. Mostafa, W. Ubachs, O.O. Versolato, R. Hoekstra, Cross-calibration of a combined electrostatic and time-of-flight analyzer for energy- and charge-state-resolved spectrometry of tin laser-produced plasma. *Appl. Phys. B* **128**, 39 (2021)
- R.A. Burdt, S. Yuspeh, K.L. Sequoia, Y. Tao, M.S. Tillack, F. Najmabadi, Experimental scaling law for mass ablation rate from a Sn plasma generated by a 1064 nm laser. *J. Appl. Phys.* **106**(3), 033310 (2009)
- O. Morris, A. O'Connor, E. Sokell, P. Dunne, Angular distribution of the ion emission from a tin-based laser-produced plasma extreme ultraviolet source. *Plasma Sources Sci. Technol.* **19**(2), 025007 (2010)
- A. O'Connor, O. Morris, E. Sokell, Angular and energy distribution of Sn ion debris ejected from a laser-produced plasma source, for laser power densities in the range suitable for extreme ultraviolet lithography. *J. Appl. Phys.* **109**(7), 073301 (2011)
- A.Z. Giovannini, N. Gambino, B. Rollinger, R.S. Abhari, Angular ion species distribution in droplet-based laser-produced plasmas. *J. Appl. Phys.* **117**(3), 033302 (2015)
- S. Fujioka, H. Nishimura, K. Nishihara, M. Murakami, Y.G. Kang, Q. Gu, K. Nagai, T. Norimatsu, N. Miyanaga, Y. Izawa, K. Mima, Y. Shimada, A. Sunahara, H. Furukawa, Properties of ion debris emitted from laser-produced mass-limited tin plasmas for extreme ultraviolet light source applications. *Appl. Phys. Lett.* **87**(24), 241503 (2005)
- D. Kurilovich, A.L. Klein, F. Torretti, A. Lassise, R. Hoekstra, W. Ubachs, H. Gelderblom, O.O. Versolato, Plasma propulsion of a metallic microdroplet and its deformation upon laser impact. *Phys. Rev. Appl.* **6**(1), 014018 (2016)
- B. Liu, R. Meijer, J. Hernandez-Rueda, D. Kurilovich, Z. Mazzotta, S. Witte, O.O. Versolato, Laser-induced vaporization of a stretching sheet of liquid tin. *J. Appl. Phys.* **129**(5), 1 (2021)
- S. Reijers, D. Kurilovich, F. Torretti, H. Gelderblom, O.O. Versolato, Laser-to-droplet alignment sensitivity relevant for laser-produced plasma sources of extreme ultraviolet light. *J. Appl. Phys.* **124**(1), 013102 (2018)
- R. Schupp, F. Torretti, R. Meijer, M. Bayraktar, J. Scheers, D. Kurilovich, A. Bayerle, K. Eikema, S. Witte, W. Ubachs, R. Hoekstra, O.O. Versolato, Efficient generation of extreme ultraviolet light from Nd:YAG-driven microdroplet-tin plasma. *Phys. Rev. Appl.* **12**(1), 014010 (2019)
- F. Torretti, F. Liu, M. Bayraktar, J. Scheers, Z. Bouza, W. Ubachs, R. Hoekstra, O.O. Versolato, Spectral characterization of an industrial EUV light source for nanolithography. *J. Phys. D* **53**(3), 055204 (2019)
- D. Hemminga, L. Poirier, M. Basko, R. Hoekstra, W. Ubachs, O.O. Versolato, J. Sheil, High-energy ions from Nd:YAG laser ablation of tin microdroplets: Comparison between experiment and a single-fluid hydrodynamic model. *Plasma Sources Sci. Technol.* **30**, 105006 (2021)
- Y. Sakai, I. Katsumata, An energy resolution formula of a three plane grids retarding field energy analyzer. *Jpn. J. Appl. Phys.* **24**, 337 (1985)